





## Experimental and theoretical study of the $^{65}\text{Cu}(n, p)^{65}\text{Ni}$ reaction cross section from reaction threshold up to 25 MeV

R. K. Singh <sup>1,\*</sup>, N. L. Singh<sup>1,5,\*</sup>, Mayur Mehta<sup>1,2</sup>, Rakesh Chauhan <sup>1</sup>, H. Kumawat,<sup>3</sup> Rajnikant Makwana <sup>1</sup>, S. V. Suryanarayana <sup>3</sup>, B. K. Nayak,<sup>3</sup> H. Naik,<sup>4</sup> Jan Varmuza,<sup>6</sup> and K. Katovsky<sup>6</sup>

<sup>1</sup>*Department of Physics, Faculty of Science, The M. S. University of Baroda, Vadodra 390002, India*

<sup>2</sup>*Institute for Plasma Research, Gandhinagar, Gujarat 382428, India*

<sup>3</sup>*Nuclear Physics Division, Bhabha Atomic Research Centre, Mumbai 400085, India*

<sup>4</sup>*Radiochemistry Division, Bhabha Atomic Research Centre, Mumbai 400085, India*

<sup>5</sup>*Department of Physics, Netaji Subhas University of Technology, Dwarka, Delhi 110078, India*

<sup>6</sup>*Department of Electrical Power Engineering, Brno University of Technology, Brno 61600, Czech Republic*



(Received 30 April 2022; accepted 6 April 2023; published 15 May 2023)

The cross section of the  $^{65}\text{Cu}(n, p)^{65}\text{Ni}$  reaction was studied experimentally at three different neutron energies using an activation technique. The quasimonoeenergetic neutrons were produced via the  $^7\text{Li}(p, n)$  reaction at the 14UD BARC-TIFR Pelletron facility in Mumbai, India. Al monitor foils along with Cu samples were activated to determine the incident neutron flux. The activities of the reaction products were measured using a high resolution high purity germanium spectrometry system. Statistical model calculations were performed using the reaction codes TALYS (ver. 1.9) and EMPIRE (ver. 3.2.3) from the reaction threshold to the neutron energy of 25 MeV. Additionally, the effects of various combinations of the theoretical nuclear level densities (NLDs), optical model potentials (OMPs), preequilibrium models (PEs), and  $\gamma$ -ray strength functions ( $\gamma$  SFs) were considered for the reproduction of experimental data. The input parameters needed in theoretical calculations to reproduce the present and previous measurements were taken from the RIPL-3 database. The present results are compared with the previous measurements, with the latest evaluations of the ENDF/B-VIII.0, JEFF-3.3, JENDL-4.0/HE, CENDL-3.2, TENDL-2019, and FENDL-3.2 libraries, and with the theoretically calculated values based on TALYS and EMPIRE codes. Furthermore, the cross section of the  $^{65}\text{Cu}(n, p)^{65}\text{Ni}$  reaction was estimated within the neutron energies of 14–15 MeV using different systematic formulas. These estimated cross sections by various systematic formulas were compared with the available experimental data. The present data will help to understand the nuclear reaction theory (models) in higher energy regions and improve the evaluated nuclear data evaluation that is needed for fundamental nuclear applications.

DOI: [10.1103/PhysRevC.107.054607](https://doi.org/10.1103/PhysRevC.107.054607)

### I. INTRODUCTION

The use of copper as a first wall material has been considered in reactor designs that have high thermal loads on the first wall or require a shield of high electrically conductive material surrounding the plasma to help stabilize its location. Other designs also use copper as a heat sink with other materials for highly loaded diverter collector plates. Copper alloys are also considered for the electrically conducting central column of the close aspect ratio tokamaks for the new concept of compact fusion machines [1]. The ones that generate gaseous elements such as hydrogen and helium by the  $(n, xp)$  and  $(n, x\alpha)$  reactions are of prime concern for studying the structural stability of reactor materials from the multiple neutrons induced reactions that take place within a fusion reactor. These reactions cause damage to the first wall and structural and blanket material of the fusion reactor. In addition, other processes such as atomic displacements and transmutations

may create microstructural defects and the processing of hydrogen and helium changes the physical properties of the products [2].

In addition, the study of the neutron induced reactions  $(n, \gamma)$ ,  $(n, p)$ ,  $(n, \alpha)$ ,  $(n, 2n)$ , etc., on different nuclei provides an experimental archive to assess the relevance of the theoretical models of nuclear physics for practical applications. The experimental results help to evaluate the statistical model code and limit the parameter set used therein. Such studies can also provide valuable insight into the reaction mechanisms that dominate different regions of energy. It should be noted that updating the evaluated cross sections depends on the availability of accurate measurements obtainable from advanced neutron sources. For a given  $(n, xp)$  reaction, the contributions of the direct, preequilibrium, and statistical compound nucleus processes to the emission of charged particles can be estimated [3,4]. For the analysis of the nuclear structure and the reaction mechanisms, the precise calculations of neutron induced reaction cross sections of different materials within a wide range of neutron energy are essential. Nuclear data are very important in nuclear technology research, such as the

\*ratankumar339@gmail.com; nl.singh-phy@msubaroda.ac.in

TABLE I. Summary of the  $^{65}\text{Cu}(n, p)^{65}\text{Ni}$  reaction cross sections from the previous measurements.

Sample form	Decay data	Detector	Monitor reaction	Neutron source	Reference
Cu metal sheet	$E_\gamma = 1481.84, I_\gamma = 23.59$ $\tau_{1/2} = 2.5175$ h	HPGe (30% relative efficiency)	$^{27}\text{Al}(n, \alpha)^{24}\text{Na}$	$\text{T}(d, n)^4\text{He}$	Gandhi [7]
Cu metal	$E_\gamma = 1115.5, I_\gamma = 15.43$ $\tau_{1/2} = 2.5175$ h	HPGe (24.7% relative efficiency)	$^{93}\text{Nb}(n, 2n)^{92\text{m}}\text{Nb}$	$\text{T}(d, n)^4\text{He}$	Filatenkov [8]
CuO	$E_\gamma = 1481.8, I_\gamma = 23.59$ $\tau_{1/2} = 2.5175$ h	HPGe	$^{115}\text{In}(n, n')^{115\text{m}}\text{In}$	$\text{D}(d, n)^3\text{He}$	Furutaa [9]
Cu	$E_\gamma = 1481.8, I_\gamma = 23.59$ $\tau_{1/2} = 2.5172$ h	HPGe (70% efficiency)	$^{27}\text{Al}(n, \alpha)^{24}\text{Na}$	$\text{D}(d, n)^3\text{He}$	Mannhart [10]
CuO	$E_\gamma = 1115.5, I_\gamma = 15.2$ $\tau_{1/2} = 2.52$ h	Ge(Li)	$^{27}\text{Al}(n, \alpha)^{24}\text{Na}$	$\text{T}(d, n)^4\text{He}$	Harun-Ar-Rashid [11]
CuO	$E_\gamma = 1481.8, I_\gamma = 23.59$ $\tau_{1/2} = 2.5175$ h	HPGe (22% efficiency)	$^{115}\text{In}(n, n')^{115\text{m}}\text{In}$	$\text{D}(d, n)^3\text{He}$	Shimizua [12]
Cu metal	$E_\gamma = 1481.8, I_\gamma = 23.59$ $\tau_{1/2} = 2.5175$ h	Germanium intrinsic detector	$^{27}\text{Al}(n, \alpha)^{24}\text{Na}$	$^9\text{Be}(p, n)$	Uwamino [21]
Cu	$E_\gamma = 1115.84$ $I_\gamma = 15.134, \tau_{1/2} = 2.52$ h	Ge(Li)	$^{27}\text{Al}(n, \alpha)^{24}\text{Na}$	$\text{T}(d, n)^4\text{He}$	Ikeda [14]
Cu	$E_\gamma = 1481, I_\gamma = 23.59$ $\tau_{1/2} = 2.56$ h	Ge(Li)	$^{27}\text{Al}(n, \alpha)^{24}\text{Na}$	$\text{T}(d, n)^4\text{He}$	Ngoc [15]
Cu	$E_\gamma = 1481.8, I_\gamma = 23.59$ $\tau_{1/2} = 2.5175$ h	Sodium-iodide crystal	$^{56}\text{Fe}(n, p)^{56}\text{Mn}$	$\text{T}(d, n)^4\text{He}$	Ryves [16]
Cu	$E_\gamma = 1482, I_\gamma = 23.5$ $\tau_{1/2} = 2.52$ h	Ge(Li)	$^{27}\text{Al}(n, \alpha)^{24}\text{Na}$	$\text{T}(d, n)^4\text{He}$	Molla [13]
Cu	$E_\gamma = 1115, I_\gamma = 16$ $\tau_{1/2} = 2.564$ h	Sodium-iodide crystal	$^{65}\text{Cu}(n, 2n)^{64}\text{Cu}$	$\text{T}(d, n)^4\text{He}$	Maslov [17]
Cu	$E_\gamma = 1483, I_\gamma = 25$ $\tau_{1/2} = 2.55$ h	Ge(Li)	$^{56}\text{Fe}(n, p)^{56}\text{Mn}$	$\text{T}(d, n)^4\text{He}$	Clator [18]
Cu	$E_\gamma = 1490, I_\gamma = 23.59$ $\tau_{1/2} = 2.56$ h	Sodium-iodide crystal	$^{32}\text{S}(n, p)^{32}\text{P}$	$\text{T}(p, n)$ $\text{D}(d, n)^3\text{He}$ $\text{T}(d, n)^4\text{He}$	Santry [19]
Cu	$E_\gamma = 1490, I_\gamma = 25$ $\tau_{1/2} = 2.6$ h	Boric acid counter	$^{27}\text{Al}(n, \alpha)^{24}\text{Na}$	$\text{T}(d, n)^4\text{He}$	Bormann [20]

design of fusion devices, fission power plants, accelerators, environment, space dosimetry, material analysis, and isotopes production. All the applications are covered by the range of neutron induced reaction cross sections [5].

Several authors studied the  $(n, p)$  reaction cross section of the  $^{65}\text{Cu}$  isotope as mentioned in Table I. These experimental cross-section data are reported in the EXFOR database [6] and were measured using neutrons from the D-D and D-T reactions [7–20], whereas only one datum in the quasimonoenergetic neutrons was produced based on  $^9\text{Be}(p, n)$  reaction neutrons [21]. The existing experiment and evaluation of the  $^{65}\text{Cu}(n, p)^{65}\text{Ni}$  reaction from threshold to 20 MeV are shown in Fig. 1. These available experimental data agree very well with each other below 12 MeV but reveal huge discrepancies in the cross section above 13 MeV. There are also significant differences in the evaluated  $(n, p)$  reaction cross section of the  $^{65}\text{Cu}$  isotope above the neutron energy of 14 MeV, which were found in many Evaluated Nuclear Data File (ENDF) libraries [22–27]. Due to the significant

spread in the measured cross-section values, it is not surprising that the evaluated  $^{65}\text{Cu}(n, p)^{65}\text{Ni}$  reaction cross section varies significantly above the neutron energies of 12 MeV, making it very uncertain extrapolating to higher energies. The significant discrepancies in the measured  $(n, p)$  reaction cross section above 12 MeV were the main reason for the present study at higher energies.

In the present paper, the cross section of the  $^{65}\text{Cu}(n, p)^{65}\text{Ni}$  reaction was measured above 13 MeV incident neutron energies relative to the  $^{27}\text{Al}(n, \alpha)^{24}\text{Na}$  [28] reference reaction by activation and offline  $\gamma$ -ray spectrometric technique. The present results were compared with the experimental data taken from the EXFOR database and evaluations of the ENDF/B-VIII.0, JEFF-3.3, JENDL-4.0/HE, CENDL-3.2, TENDL-2019, and FENDL-3.2 [22–27] libraries. The statistical nuclear reaction TALYS (ver. 1.9) [29] and EMPIRE (ver. 3.2.3) [30] codes were used to calculate the cross sections using different optical potential, level density, and preequilibrium model options as given in the codes. In theoretical

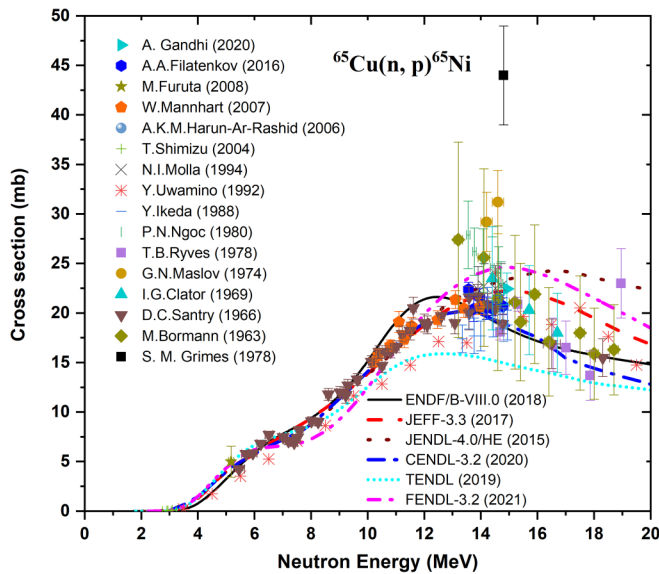


FIG. 1. The previous experimental cross section from EXFOR and evaluated from the ENDF/B-VIII.0, JEFF-3.3, JENDL-4.0/HE, CENDL-3.2, TENDL-2019, and FENDL-3.2 libraries for the  $^{65}\text{Cu}(n, p)^{65}\text{Ni}$  reaction cross section from the reaction threshold to 20 MeV.

calculations from statistical codes, suitable model selection is essential to obtain the correct reaction cross-section values. In addition, the  $(n, p)$  reaction cross section of the  $^{65}\text{Cu}$  isotope was calculated using the systematic formulas of different authors within 14–15 MeV neutron energies and the results are compared with the previous experimental data.

## II. EXPERIMENTAL PROCEDURE

The  $^{65}\text{Cu}(n, p)^{65}\text{Ni}$  reaction cross section was measured using the activation technique with the neutron energies of 13.52, 16.86, and 19.89 MeV. The irradiations of the samples were performed at the 14UD Pelletron accelerator facility of Bhabha Atomic Research Centre and Tata Institute of Fundamental Research (BARC-TIFR) in Mumbai, India. These neutrons were produced via the  $^7\text{Li}(p, n)$  reaction ( $E_{\text{th}} = 1.88$  MeV) using the protons of 16, 19, and 22 MeV. The average proton beam current was  $\approx 180$  nA during sample irradiation and proton energy spreads at the 6-m port elevation level (above the analyzing magnet) were 50–90 keV. Initially, the proton was accelerated inside a 6-mm-diameter collimator and hit on the natural lithium (Li) foil of a thickness of  $\approx 6.8$  mg/cm<sup>2</sup>, which was sandwiched between the two tantalum (Ta) foils. The front tantalum foil which faced the proton beam is the thinnest one with a thickness of  $\approx 4$  mg/cm<sup>2</sup>, whereas the proton beam stop was served by a 0.1-mm-thick layer of tantalum. The energy loss of the 16, 19, and 22 MeV proton in the primary targets lithium and tantalum were calculated by the Monte Carlo simulation code SRIM-2008 [31], and the values are 177 to 137 keV in the Li foil and 54 to 44 keV in the Ta foil. The pressure inside the 6-m port was  $8 \times 10^{-8}$  torr, whereas it was atmospheric in the neutron activation zone. The sample holder was placed at 0°

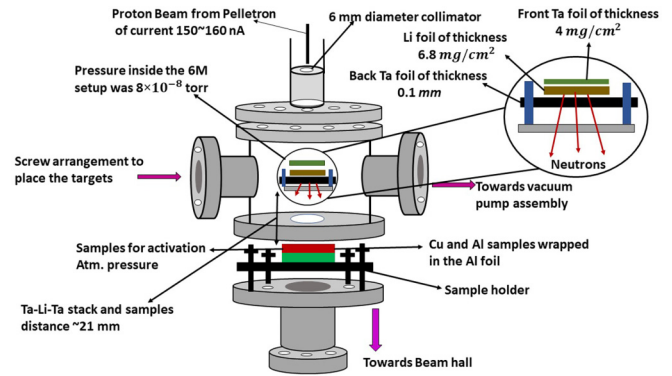


FIG. 2. The schematic diagram of the experimental setup for neutron irradiation of the samples.

with respect to the incident proton beam direction at 21 mm from the Ta-Li-Ta targets configuration. This experimental setup for neutron irradiation is shown in Fig. 2. The neutron flux for the cross-section measurements was determined by using the  $^{27}\text{Al}(n, \alpha)^{24}\text{Na}$  reference reaction. The obtained neutron flux during irradiations in the high energy region varied between  $1.48 \times 10^6$  and  $3.09 \times 10^6$  n/(cm<sup>2</sup> s). Both targets were irradiated by neutrons for 5 to 7 h to produce sufficient activity in the samples at different energies. The irradiation time along with the obtained neutron flux is given in Table II.

### A. Samples preparation

Copper in the form of the pellet was used to measure the  $^{65}\text{Cu}(n, p)^{65}\text{Ni}$  reaction cross section. The aluminum foil was used for the normalization of the neutron flux using the  $^{27}\text{Al}(n, \alpha)^{24}\text{Na}$  reference reaction cross section taken from the standard IRDFF-1.05 library. High-purity (99.5% pure) pellets of the natural copper material weight of  $\approx 0.3$  g each, 0.35-mm thickness, and an area of 1.131 cm<sup>2</sup> were prepared using a pelletizer. In addition, an aluminum metal foil (99.99% pure) of weight  $\approx 0.03$  g each, area of 1 cm<sup>2</sup>, and 0.11 mm in thickness was used along with each copper target. Microbalance equipment with the least count of 0.1 mg was used to weigh the samples. The target details used in the present experiment are given in Table III. During the irradiation process, the copper sample was sandwiched between monitor foils (Al). Each sample used for neutron irradiation was wrapped in 0.025-mm-thick aluminum foil to prevent radioactive contamination from each other.

### B. $\gamma$ -ray activity measurements

The measurements of induced activity were performed for the copper and monitor foils after the end of each irradiation using the 16% relative efficiency high purity germanium (HPGe) detector. The HPGe detector was enclosed in a heavy shield consisting of consecutive layers of lead. The irradiated samples were taken out after the cooling time of 3 to 8 h and mounted on different Perspex plates for counting in front of a lead shielded HPGe detector. These samples were placed at a distance of 3 cm from the detector window in the low

TABLE II. Summary of the irradiation, cooling, and counting times along with neutron flux and effective mean neutron energies.

$E_p$ (MeV)	$\langle E_n \rangle$ (MeV)	Neutron flux ( $n/cm^2$ s)	Irradiation time (s)	Cooling time (s)	Counting time (s)
16	$13.52 \pm 0.67$	$1.48 \times 10^6$	26700	38948	1201
19	$16.86 \pm 0.55$	$2.68 \times 10^6$	23400	12778	1202
22	$19.89 \pm 0.59$	$3.09 \times 10^6$	18900	30164	900

background counting facility of the TIFR-RCD laboratory. The relatively close geometry was used in the present paper to enhance the counting rate. At very close geometry, the correction factor related to coincidence summing effects was taken into consideration. After the irradiation, the  $\gamma$ -ray activates from the radioactive decay of  $^{65}\text{Ni}$  ( $E_\gamma = 1115.5$  keV) and  $^{24}\text{Na}$  ( $E_\gamma = 1368.6$  keV) were measured using a precalibrated HPGe detector connected to a PC based multichannel analyzer and  $\gamma$ -ray counts under each photo peak were determined by the Canberra GENIE-2000 gamma analysis software package. The detector efficiency and energy calibration were carried out using a standard and well-characterized  $^{152}\text{Eu}$  radioactive point source. The obtained energy resolution of the HPGe detector was 1.926 keV at 1408 keV  $\gamma$ -ray energy of the  $^{152}\text{Eu}$  source. The efficiency calibration curve of the HPGe detector is shown in Fig. 3. The reference latest decay data half-life of the reaction product, decay mode, energy, and intensity of  $\gamma$  lines and target isotope abundance used for the cross-section calculations are given in Table IV [32,33].

### III. DATA ANALYSIS

#### A. Neutron energy calculation

The reaction  $^7\text{Li}(p, n)$  ( $E_{\text{th}} = 1.88$  MeV) was used to produce fast monoenergetic neutrons with proton energies between 1.88 and 2.37 MeV. Above the proton energy of 2.37 MeV, the  $^7\text{Li}(p, n)$  reaction produces high energy quasimonoenergetic neutrons with some tail towards the lower energy side. This is because the first excited state of  $^7\text{Be}$  is 0.43 MeV and has a threshold of 2.37 MeV, and above these energies the first excited state is excited and produces the second group of neutrons ( $n_1$ ) along with the primary neutron ( $n_0$ ). For proton energy below 5 MeV, the zero-degree yield of these low energy neutrons is less than about 10% of the ground state yield. Thus, the usefulness of the monoenergetic neutron source is only slightly impaired. The three-body breakup reaction  $^7\text{Li}(p, n + 3\text{He})^4\text{He}$  occurs above 3.68 MeV contributing to the neutron with primary neutron peak ( $n_0$ ). The two peaks visible below the major peak correspond to the  $5/2^-$  and  $7/2^-$  resonant breakup reaction and the further lower

part of the spectra is generated from contribution to the continuum [34]. The primary neutron peak ( $n_0$ ) has higher neutron energy and flux, and this peak is used to measure the reaction cross section. The neutron spectrum from the  $^7\text{Li}(p, n)$  reaction for 16, 19, and 22 MeV was obtained using data from Refs. [35–38] by linear interpolation method. The present experiment was conducted for the natural lithium target so the contribution for  $^6\text{Li}$  was obtained using spectral shape, cross section, and neutron yields given in Ref. [37]. The contributions of  $^{6,7}\text{Li}$  were added as per natural abundance and final spectra were obtained. The threshold for  $^7\text{Li}(p, n)$  is 1.8 MeV and it is 5.9 MeV for  $^6\text{Li}(p, n)$ , therefore  $^6\text{Li}$  contributes  $\approx 2\%$  at  $E_p = 19$  MeV and  $\approx 5\%$  at  $E_p = 22$  MeV around 4 MeV below the major peak from  $^7\text{Li}$ . The contribution from  $^6\text{Li}$  is negligible at  $E_p = 16$  MeV. The neutron spectra based on the  $^{6,7}\text{Li}(p, n)$  reaction for the 16, 19, and 22 MeV proton energies are shown in Fig. 4. When using the activation technique to calculate cross sections, the low energy background neutron contribution that adds to the prominent neutron peak must be carefully measured and subtracted. We subtracted the contribution of these “background” neutrons using the Smith method [39]. The effective mean neutron energy of the primary neutron group from the spectrum was calculated using Eq. (1), and the uncertainty associated with this neutron energy was calculated from the width of the primary peak:

$$\langle E_n \rangle = \frac{\int_{E_{\text{PS}}}^{E_{\text{max}}} \Phi(E) E_i dE}{\int_{E_{\text{PS}}}^{E_{\text{max}}} \Phi(E) dE} \quad (1)$$

where  $\langle E_n \rangle$  is the effective mean neutron energy,  $E_{\text{max}}$  is the maximum neutron energy,  $E_{\text{PS}}$  is the peak forming start energy,  $E_i$  is the energy bin, and  $\phi(E)$  is the neutron flux for energy bin  $E_i$ . Using the neutron spectra, the calculated effective mean neutron energies with their uncertainties are given in Table II.

#### B. The efficiency calibration of the HPGe detector

Using the known characteristic  $\gamma$ -ray energies of the  $^{152}\text{Eu}$  point source ( $\tau_{1/2} = 13.52$  years) of known activity ( $A_0 = 6659.21$  Bq as of 1 Oct. 1999), the efficiency calibration was

TABLE III. The sample details were used for the neutron irradiation process.

Sample irradiated	Isotopes	Abundance of isotopes (%)	Sample weight (g)		Thickness (cm)	
			Cu	Al	Cu	Al
Cu metal powder	$^{65}\text{Cu}$	$30.83 \pm 0.03$	0.2152	0.0279	0.0319	0.0103
Al metal foil	$^{27}\text{Al}$		0.2511	0.0309	0.0372	0.0114
			0.2464	0.0313	0.0365	0.0116

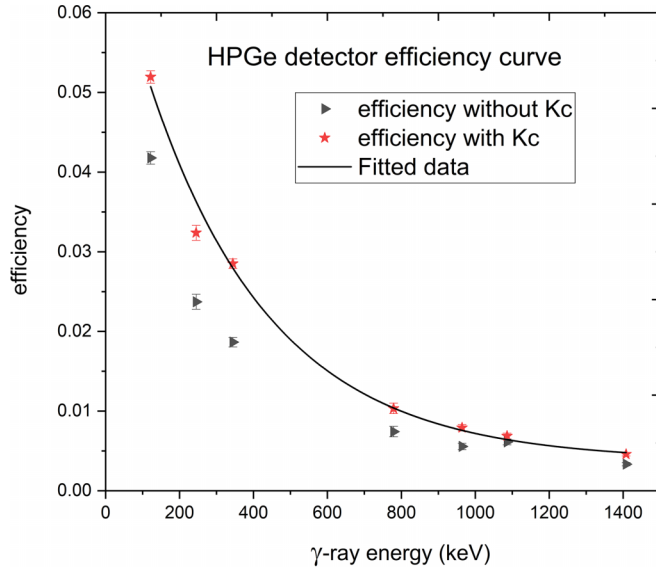


FIG. 3. The efficiency calibration curve of the HPGe detector with and without coincidence summing effect correction factor  $K_c$ .

carried out for the HPGe detector. The detector efficiency at a distance of 3 cm from the end cap of the detector for a point source was obtained by the expression

$$\varepsilon(E_\gamma) = \frac{CK_c}{N_0 I_\gamma e^{-\lambda t}} \quad (2)$$

where  $C$  is the count under  $\gamma$ -ray photo peak,  $N_0$  is the activity of the standard  $^{152}\text{Eu}$  source at the initial stage,  $I_\gamma$  is the  $\gamma$ -ray intensity,  $t$  is the elapsed time from the date of manufacture to the date of the counting,  $\lambda$  is the decay constant of the standard  $^{152}\text{Eu}$  source, and  $K_c$  is the correction factor for the coincidence summing effect. The Monte Carlo simulation code EFFTRAN [40] was used to calculate the correction factor using the HPGe detector structured data such as crystal hole cavity, end cup, mount cup, crystal material, dimension, absorber, window, and calibration source information. It is observed from Eq. (2) that the efficiency is the function of four variables ( $I_\gamma$ ,  $\lambda$ ,  $C$ ,  $N_0$ ) and uncertainty in the variables propagates in the detector efficiency. Therefore, detector efficiency can be written as the function of four  $I_\gamma$ ,  $\lambda$ ,  $C$ , and  $N_0$  attributes. The uncertainties in efficiency due to four attributes were calculated by using the quadratic sum formula

$$\left(\frac{\Delta\varepsilon_i}{\varepsilon_i}\right)^2 = \left(\frac{\Delta C_i}{C_i}\right)^2 + \left(\frac{\Delta I_\gamma}{I_\gamma}\right)^2 + \left(\frac{\Delta N_0}{N_0}\right)^2 + (t\Delta\lambda)^2. \quad (3)$$

In order to obtain the efficiencies of the characteristic  $\gamma$ -ray energies of the  $^{65}\text{Ni}$  ( $E_\gamma = 1115.53$  keV) and  $^{24}\text{Na}$  ( $E_\gamma = 1368.63$  keV), the efficiencies were interpolated through the

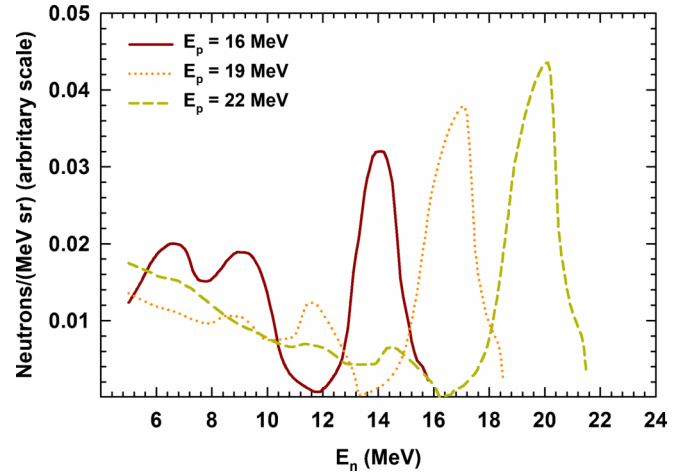


FIG. 4. Neutron spectra at 16, 19, and 22 MeV proton energies are obtained from the Refs. [34–38].

following fitting function:

$$\varepsilon(E) = \varepsilon_0 \exp(-E/E_0) + \varepsilon_c \quad (4)$$

where  $\varepsilon_0$ ,  $E_0$ , and  $\varepsilon_c$  are the fitting parameters and values given in Table V. The calculated efficiencies for characteristics  $\gamma$  lines of 1115.53 and 1368.62 keV are given in Table V.

### C. Estimation of the $^{65}\text{Cu}(n, p)^{65}\text{Ni}$ reaction cross section

The activation cross section of the  $^{65}\text{Cu}(n, p)^{65}\text{Ni}$  reaction was estimated relative to the reference  $^{27}\text{Al}(n, \alpha)^{24}\text{Na}$  monitor reaction using the standard activation equation given by

$$\langle\sigma_r\rangle = \langle\sigma_m\rangle \left( \frac{C_r \lambda_r W_m M_r A_m \varepsilon_m I_m f_m}{C_m \lambda_m W_r M_r A_r \varepsilon_r I_r f_r} \right) \times \frac{(C_{\text{attn}} C_{\text{low}} C_g)_r}{(C_{\text{attn}} C_{\text{low}} C_g)_m} \quad (5)$$

where  $r$  and  $m$  in subscript stand for sample and monitor reaction.  $\sigma$  is the reaction cross sections,  $C$  is the detected photo-peak counts of the  $\gamma$  ray of the reaction products,  $\lambda$  is the decay constant,  $\varepsilon$  is the efficiency for the characteristic  $\gamma$  ray of radionuclide,  $I$  is the  $\gamma$ -ray abundance,  $W$  is the weight,  $A$  is the isotopic abundance,  $M$  is the atomic mass,  $f$  is the time factor,  $C_{\text{low}}$  is the low energy background neutron correction factor,  $C_{\text{attn}}$  is the  $\gamma$ -ray self-attenuation correction factor, and  $C_g$  is the geometry correction factor. The timing factor as specified in Eq. (5) is given by the expression

$$f = (1 - \exp(-\lambda t_i)) \exp(-\lambda t_c) (1 - \exp(-\lambda t_m)) \quad (6)$$

where  $t_i$  is irradiation time,  $t_c$  is cooling time, and  $t_m$  is counting time. The uncertainty in the time factor  $f$  is given by the

TABLE IV. Spectroscopic decay data of the sample and monitor product nuclei with their uncertainties.

Reactions	$E_{\text{th}}$ (MeV)	Product nucleus	Half-life	Decay mode	$E_\gamma$ (keV)	$I_\gamma$ (%)
$^{65}\text{Cu}(n, p)^{65}\text{Ni}$	1.37	$^{65}\text{Ni}$	$2.5175 \pm 0.0005$ h	$\beta^-$ (100.0%)	1115.53	$15.43 \pm 0.13$
$^{27}\text{Al}(n, \alpha)^{24}\text{Na}$	3.47	$^{24}\text{Na}$	$14.997 \pm 0.012$ h	$\beta^-$ (100.0%)	1368.63	$99.9936 \pm 0.0015$

TABLE V. Measured values of fitting parameters of the HPGe detector efficiencies.

Fitting parameter	Parameter values	$E_\gamma$ (keV)	Efficiencies
$\varepsilon_0$	$0.06751 \pm 0.00373$	1115.53	0.0062
$\varepsilon_c$	$0.00377 \pm 0.0007243$	1368.63	0.00491
$E_0$	$335.39 \pm 32.384$		

expression

$$\left(\frac{\Delta f}{f}\right)^2 = \left(\frac{\lambda t_{\text{irr}} \exp(-\lambda t_{\text{irr}})}{(1 - \exp(-\lambda t_{\text{irr}}))} - \lambda t_{\text{cool}} + \frac{\lambda t_{\text{count}} \exp(-\lambda t_{\text{count}})}{(1 - \exp(-\lambda t_{\text{count}}))} - 1\right)^2 \left(\frac{\Delta \lambda}{\lambda}\right)^2.$$

The reference cross sections  $\langle \sigma_m \rangle$  of the monitor reaction  $^{27}\text{Al}(n, \alpha)^{24}\text{Na}$  were obtained using the International Reactor Dosimetry and Fusion File (IRDF-1.05) database with the neutron flux energy spectrum. The  $^{27}\text{Al}(n, \alpha)^{24}\text{Na}$  reaction cross section known with an accuracy of 0.4–0.8%, was used for the neutron fluence determination as to the reference data. The spectrum averaged cross sections were  $\langle \sigma_m \rangle$  obtained by the following relation:

$$\langle \sigma_m \rangle = \frac{\sum \varphi_0 \sigma_m(E) dE}{\sum \varphi_0 dE}. \quad (7)$$

The neutron flux during the irradiation process was calculated using the equation given below:

$$\langle \Phi \rangle = \left(\frac{C_m \lambda_m}{\langle \sigma_m \rangle N \varepsilon_m I_m f_m}\right) \times (C_{\text{attn}} C_{\text{low}} C_g). \quad (8)$$

The calculated spectrum averaged cross sections with their uncertainties are given in Table VI.

#### D. Estimation of the correction factor and uncertainties

The interaction of the  $\gamma$  rays with materials requires the correction of the self-attenuation effect. Beer-Lambert's law gives a correction factor for the  $\gamma$ -ray self-attenuation factor  $\Gamma_{\text{attn}}$  for activated materials, which was calculated by following relation  $C_{\text{attn}} = (1 - e^{-\mu l})/(\mu l)$  where  $l$  is the thickness of the materials and  $\mu$  is the mass attenuation coefficient of the  $\gamma$ -ray energy and material, which was calculated from XMuDat (ver.1.0.1) [41]. The correction factor for the counting geometry is given by the expression

$$C_g = (D + h/2)^2 / D^2 \quad (9)$$

TABLE VI. Measured  $^{65}\text{Cu}(n, p)^{65}\text{Ni}$  reaction cross-section values relative to standard  $^{27}\text{Al}(n, \alpha)^{24}\text{Na}$  reaction cross sections with uncertainties.

$\langle E_n \rangle \pm \Delta E_n$ (MeV)	$^{27}\text{Al}(n, \alpha)^{24}\text{Na}$ (mb)	$^{65}\text{Cu}(n, p)^{65}\text{Ni}$ (mb)
$13.52 \pm 0.67$	$121.54 \pm 0.242$	$22.24 \pm 2.86$
$16.86 \pm 0.55$	$80.98 \pm 0.162$	$14.56 \pm 2.66$
$19.89 \pm 0.59$	$41.73 \pm 0.194$	$12.61 \pm 2.71$

TABLE VII. The measured values of the correction factor of the low energy background neutron, geometry, and self-attenuation.

$\langle E_n \rangle \pm \Delta E_n$ (MeV)	$\Gamma_{\text{attn}}$		$C_{\text{low}}$		$C_g$	
	Cu	Al	Cu	Al	Cu	Al
$13.52 \pm 0.67$	0.99202	0.99929	0.6541	0.5646	1.0107	1.0034
$16.86 \pm 0.55$	0.99071	0.99922	0.5883	0.5735	1.0124	1.0038
$19.89 \pm 0.59$	0.99088	0.99915	0.3937	0.4814	1.0122	1.0039

where  $h$  is the thickness of the sample and  $D$  is the distance from the measured sample to the surface of the Ge crystal. The spectral indexing method correction for low energy background neutron subtraction is given in Ref. [39]. The following relation subtracted the correction for the low energy background neutron ( $p, n_1$ ):

$$C_{\text{low}} = 1 - \frac{\int \phi(E_{p_1}) \sigma_i(E_{p_1})}{\int \phi(E) \sigma_i(E) dE} \quad (10)$$

where  $E_{p_1}$  and  $E_{p_2}$  are primary and secondary neutron energy peaks in the neutron flux spectrum,  $\phi(E) = \phi(E_{p_1}) + \phi(E_{p_2})$  is the neutron flux, and  $\sigma_i(E)$  is the reaction cross sections. The cross section  $\sigma_i(E)$  of the  $^{65}\text{Cu}(n, p)^{65}\text{Ni}$  reaction was taken from the evaluated data of the ENDF/B-VIII.0 [22] library and for the  $^{27}\text{Al}(n, \alpha)^{24}\text{Na}$  reaction was taken from the IRDF-1.05 library [28]. The IRDF-1.05 library seems to be most preferable for this purpose because this evaluation is one of the latest and contains detailed information on both cross sections and uncertainties. The correction factors used in the cross-section calculation are given in Table VII.

The uncertainties in the measured cross sections arise from the counting statistics of the detected photo-peak counts of the  $\gamma$  rays of the reaction products of both the copper sample and the aluminum monitor. The uncertainties associated with the measured cross sections include uncertainties in (i) monitor cross sections, (ii) counting statistics, (iii) detector efficiency, (iv)  $\gamma$ -ray self-absorption, (v) atomic mass, (vi) decay data, (vii) weight, and (viii) time factor. Total uncertainties were estimated in quadrature by taking the square root of the sum of the squares of the individual uncertainties. The compilation of the uncertainties in the present measured data is listed in Table VIII.

#### IV. THEORETICAL CALCULATIONS

The theoretical estimations of the  $^{65}\text{Cu}(n, p)^{65}\text{Ni}$  reaction cross section were executed using the TALYS [29] and EMPIRE [30] codes from reaction threshold to 25 MeV neutron energy. These two are the statistical reaction codes including direct reaction, preequilibrium emission (PE), and compound nucleus (CN) reaction mechanisms. The present results as well as the previous ones were compared with the theoretically calculated values based on the TALYS and EMPIRE codes.

TABLE VIII. Compilation of the uncertainties (%) in the measured cross section of the present paper.

Uncertainties	Sample (Cu)	Monitor reaction (Al)
Monitor cross section		0.2–0.5
Counting statistics	15	5
Detector efficiency	2	1.43
$\gamma$ -ray self-absorption	<1	<1
Atomic mass	0.008	0.01
Half-life	0.02	0.08
Weight	0.02	0.02
Abundance	0.09	
$\gamma$ -ray intensity	0.84	0.15
Time factor	0.5	0.5

### A. Calculation of the reaction cross section using the TALYS code

The calculation of cross sections using the TALYS code contributes to the compound nucleus by the Hauser-Feshbach theory [42]. The preequilibrium contribution models based on the exciton model [43] and multistep compound (MSC) and multistep direct (MSD) [44] were used in the calculations. In the direct reaction calculation, the default option used is the coupled channels model. In addition, the optical potential mentioned by Koning-Delaroche [45] and Bauge-Delaroche [46] was used to obtain optical model parameters for neutrons and protons from the RIPL-3 [47] database. To consider the  $\gamma$ -ray emission channel competition in reaction, TALYS uses a fixed  $\gamma$ -ray strength function model. The Brink-Axel Lorentzian [48–49] was implemented for the  $\gamma$ -ray strength functions for all the transitions and the Kopecky-Uhl generalized Lorentzian [50] is used for the  $E1$  transitions.

The six different phenomenological and microscopic nuclear level density models are used for the estimation of nuclear reaction cross section. These models range from phenomenological analytical expressions to tabulated level densities derived from microscopic models. The phenomenological level density models are as follows:

(i) In the constant temperature model introduced by Gilbert-Cameron [51], the excitation energy is divided into two-parts: the lower energy part where the constant temperature law applies and the higher energy part where the Fermi gas model applies.

(ii) In the back-shifted Fermi gas model [52], the Fermi gas expression is used in all the excitation energy regions.

(iii) In the generalized superfluid model [53–54], superconductive pairing correlations are considered according to the Barden-Cooper-Schrieffer theory, i.e., low energy pairing correlations strongly influence the level density. In contrast, the high energy region is described by the Fermi gas model.

The other three microscopic level density models are as follows.

(i) In ldmodel 4 for the RIPL database, Goriely has calculated level densities from drip line to drip line based on Hartree-Fock calculations for excitation energies up to 150 MeV and spin values up to  $I = 30$  [55].

TABLE IX. The experimental value of  $D_0$  for the  $^{65}\text{Cu}$  was obtained from the RIPL-3 database and compared with the theoretical values predicted for each level density model by the TALYS code.

Level density model	Experimental value of $D_0$ (keV)	Theoretical value of $D_0$ (keV)
Constant temperature	$1.3 \pm 0.11$	0.3179
Back-shifted Fermi gas		0.6025
Generalized superfluid		0.5758
Goriely (microscopic 1)		0.7782
Goriely-Hilaire (microscopic 2)		0.4051
Goriely-Hilaire Gogny force (microscopic 3)		0.6720

(ii) In ldmodel 5 the calculations make coherent use of nuclear structure properties determined within the deformed Skyrme-Hartree-Fock-Bogoliubov framework [56].

(iii) The ldmodel 6 is based on temperature-dependent Hartree-Fock-Bogoliubov calculations using the Gogny force [57]. The  $D_0$  is  $s$ -wave average neutron resonance spacing in keV at the neutron separation energy and it is related to the level density according to the following formula:

$$\frac{1}{D_0} = \sum_{J=|I-\frac{1}{2}|}^{J=|I+\frac{1}{2}|} \rho(S_n, J, \Pi). \quad (11)$$

The experimental value of  $D_0$  for the  $^{65}\text{Cu}$  was obtained from the RIPL-3 database [47] and compared with the theoretical values predicted for each level density model by TALYS code. The values of the  $D_0$  are mentioned in Table IX.

The parameter  $\alpha$  is the energy dependent level density parameter, which considers the existence of shell effects at low energies and the damping of the latter as the excitation energy increases according to the following equation:

$$\alpha = \alpha(E_x) = \hat{\alpha} \left( 1 + \delta W \left( \frac{1 - \exp(-\gamma U)}{U} \right) \right). \quad (12)$$

The terms  $\delta W$  and  $\gamma$  stand for the shell correction energy and the damping parameter of shell effects with increasing excitation energy, respectively. The parameter  $\hat{\alpha}$  is called the asymptotic level density parameter and is equal to  $\alpha$  when shell effects are absent.

The level density models with default input parameters were not viable for producing cross sections that agree well with the experimental data taken from the EXFOR database. Therefore, various input parameters are adjusted in the TALYS code to reproduce the admissible cross sections for the entire neutron energy range. It is assumed that nuclear reactions are dependent on the nuclear level densities (NLDs), optical model potentials (OMPs), and  $\gamma$ -ray strength functions ( $\gamma$  SFs). The description of the different theoretical models is given in Table X. The preequilibrium contribution, which becomes essential for incident energies above almost 10 MeV is modeled using the two-component exciton model. The combinations for input parameters were considered to determine

TABLE X. The statistical model codes used for the theoretical calculations of the  $^{65}\text{Cu}(n, p)^{65}\text{Ni}$  reaction cross section.

Statistical codes	Optical potential model	Level density models	Preequilibrium model	$\gamma$ -ray strength function model
EMPIRE	Koning-Delaroche	Generalized superfluid Gilbert-Cameron Hartree-Fock-BCS	Multistep compound Multistep direct Exciton model (PCROSS) Monte Carlo hybrid (DDHMS)	Modified Lorentzian (MLO1)
TALYS	Koning-Delaroche local Koning-Delaroche global Koning-Delaroche dispersive Bauge-Delaroche	Constant temperature Back-shifted Fermi gas Generalized superfluid Goriely Goriely-Hilaire Goriely-Hilaire Gogny force	Exciton model Multistep compound Multistep direct	Kopecky-Uhl strength 1: Kopecky-Uhl generalized Lorentzian

the theoretical variation in cross sections and the sensitivity of the cross sections to each nuclear model.

### B. Calculation of the reaction cross section using the EMPIRE code

In addition, the theoretical calculations were performed using the EMPIRE [30] code. In the EMPIRE code, the CN reaction cross section was calculated in the framework of the Hauser-Feshbach theory [42]. The calculation of the direct reaction was considered using the ECIS06 code [58]. The width fluctuation corrections were considered using the Hofmann, Richert, Tepel, and Weidenmuller model [59–61] up to an incident neutron energy of 3 MeV. The optical potential model parameters for the outgoing protons were also taken from the RIPL-3 [47] database using Koning and Delaroche [45]. The  $\gamma$ -ray strength function was described via the modified Lorentzian model [62] available in the RIPL-3 database. The different level density models, namely, (i) Gilbert-Cameron [51], (ii) generalized superfluid [53–54], and (iii) Hartree-Fock-BCS approach [55], were used for estimating the cross sections from threshold to 25 MeV. Moreover, the quantum-mechanical preequilibrium models (i) MSC [63] and (ii) MSD [64] and the phenomenological preequilibrium models (i) exciton model with default mean free path multiplier (PCROSS = 1.5) [65] and (ii) Monte Carlo hybrid (DDHMS) [66] were implemented to consider the preequilibrium emission at higher energies in the  $^{65}\text{Cu}(n, p)^{65}\text{Ni}$  reaction cross section.

### V. SYSTEMATIC FORMULAS FOR THE CALCULATION OF THE $(n, p)$ REACTION CROSS SECTION FOR THE $^{65}\text{Cu}$ ISOTOPE

It is observed that for many nuclei a systematic experimental study of 14 MeV neutron induced charged particle reaction cross sections such as  $(n, p)$  and  $(n, \alpha)$  was performed over the years. For many uses, such as studying structural materials of fusion reactors and neutron dosimetry, precise cross sections around 14–15 MeV neutrons are essential for refining nuclear theory. In several areas, the need for fast neutron induced reaction cross-section data has increased, for example, in biomedical applications such as radioisotopes

manufacturing and cancer treatment; accelerator-driven incineration/transmutation of long-lived radioactive nuclear waste (in specific transuranium nuclides) into short-lived or stable isotopes of secondary spallation neutrons produced by high-intensity and intermediate-energy charged-particle beams; prolonged planetary space missions; shielding for particle accelerators; and material irradiation experiments concerning research and development for fusion reactor technology. Several authors have also suggested several empirical and semiempirical formulas with various parameters for measurements of  $(n, p)$  reaction cross sections.

In the present paper, the systematic formulas suggested by various authors were used to estimate the  $(n, p)$  reaction cross section for the  $^{65}\text{Cu}$  isotope [67–77]. The calculated cross sections were compared with the previous measurements near 14.5 MeV neutron energies. Various systematic formulas for the  $(n, p)$  reaction are given in Table XI, whereas values of calculated reaction cross sections are also given in Table XI. It is observed that the  $(n, p)$  reaction cross section decreases as a function of mass number. The  $(n, p)$  reaction cross sections of the  $^{65}\text{Cu}$  isotope estimated by systematic formulas of Habbani and Tel are in better agreement with the previous measurements of the  $^{65}\text{Cu}$  isotope.

### VI. RESULTS AND DISCUSSIONS

The cross sections of the  $^{65}\text{Cu}(n, p)^{65}\text{Ni}$  reaction at 13.52, 16.86, and 19.89 MeV neutron energies as measured in the present paper along with their uncertainties are given in Table VI. Theoretical calculations were performed using the TALYS and EMPIRE codes, first with a default parameter and then with possible parameter adjustments. The present results were compared with the statistical model calculations, the latest evaluations, and the data from the previous measurements. Both theoretical codes included several OMPs, NLDs, PEs, and  $\gamma$ SFs models as listed in Tables XII and XIII.

#### A. Comparison of experimental and evaluation data

The present measurement of the  $^{65}\text{Cu}(n, p)^{65}\text{Ni}$  reaction cross section is shown in Fig. 5 along with the literature data taken from the EXFOR compilation [6] and the evaluated data from ENDF/B-VIII.0, JEFF-3.3, JENDL-4.0/HE, CENDL-



TABLE XI. Systematic formulas for the  $(n, p)$  reaction and calculated cross sections for the  $^{65}\text{Cu}$  isotope [67–77].

Authors	Formulas for the $(n, p)$ cross section	Mass region	Cross sections (mb)
Luo	$\sigma_{n,p} = 62.98(A^{\frac{1}{3}} + 1)^2 \exp(-34.45 \frac{(N-Z)}{A})$	$46 \leq A \leq 196$	38.86
Forrest	$\sigma_{n,p} = 900(A^{\frac{1}{3}} + 1)^2 \exp(-49.27 \frac{(N-Z)}{A} + 197.1 \frac{(N-Z)^2}{A^2} - 0.45A^{\frac{1}{2}})$	$40 \leq A \leq 187$	29.41
Tel	$\sigma_{n,p} = 7.31(A^{\frac{1}{3}} + 1)^2 \exp(\frac{-20.21(N-Z)}{A})$	$17 \leq A \leq 239$ odd-Z, even-N	20.91
Habbani	$\sigma_{n,p} = 20.91(A^{\frac{1}{3}} + 1)^2 \exp(-29.53 \frac{(N-Z)}{A})$	$29 \leq A \leq 209$ Odd A	21.94
	$\sigma_{n,p} = 60.34(A^{\frac{1}{3}} + 1)^2 \exp(-34.44 \frac{(N-Z+1)}{A})$	$28 \leq A \leq 208$ Even A	
Doczi	$\sigma_{n,p} = 18.12(A^{\frac{1}{3}} + 1)^2 \exp(-19.61 \frac{(N-Z)}{A} + \frac{(N-Z)^2}{A^2})$	$28 \leq A \leq 209$	54.64
Kasugai	$\sigma_{n,p} = 1264(N-Z+1) \exp(\frac{-46.63(N-Z+1)}{A})$	$28 \leq A \leq 187$	32.54
Konno	$\sigma_{n,p} = 31.42(A^{\frac{1}{3}} + 1)^2 \exp(\frac{-29.07(N-Z)}{A})$	$40 \leq A \leq 209$	34.60
Kumabe	$\sigma_{n,p} = 21.8A \exp(\frac{-34(N-Z)}{A})$	$40 \leq A \leq 62$	36.41
Ait-Tahar	$\sigma_{n,p} = 90.68(A^{\frac{1}{3}} + 1)^2 \exp(\frac{-34.48(N-Z+1)}{A})$	$40 \leq A \leq 187$	32.81
Bychkov	$\sigma_{n,p} = 7.06\pi r_0^2 (A^{\frac{1}{3}} + 1)^2 \exp(\sqrt{\frac{a}{E_n}} (\frac{0.58(Z-1)}{A} - \frac{50(N-Z+1)}{A}) - 3.26)$	$28 \leq A \leq 209$	17.07
Levkovski	$\sigma_{n,p} = 50.21(A^{\frac{1}{3}} + 1)^2 \exp(\frac{-33.8(N-Z)}{A})$	$40 \leq A \leq 209$	33.23

TABLE XII. The TALYS adjusted model calculations with different statistical models and parameters.

Optical potential model	Level density models	Preequilibrium model	widthmode	Parameters
Koning-Delaroche local	Constant temperature	preeqmode 3	2	asys y gshell y a 28 65 10.999
Koning-Delaroche dispersive	Back-shifted Fermi gas	preeqmode 3	2	asys y deltaW 28 65 1.1
Koning-Delaroche global	Generalized superfluid	preeqmode 3	2	asys y deltaW 28 65 1.61
Koning-Delaroche global	Goriely	preeqmode 3	2	ptable 28 65 1.123
Koning-Delaroche global	Goriely-Hilaire	preeqmode 3	2	ctable 28 65 0.705 ptable 28 65 0.833
Koning-Delaroche global	Goriely-Hilaire Gogny force	preeqmode 3	2	asys y gshell y ctable 28 65 0.705 ptable 28 65 0.833

TABLE XIII. The EMPIRE adjusted model calculations with different statistical models and parameters.

Optical potential model	Level density models	Preequilibrium model	$\gamma$ -ray strength function model	Parameters
Koning-Delaroche	Generalized superfluid	Multistep compound	Standard Lorentzian (SLO)	ATILNO 0.96 GDIV 8.0 STMRO 2.0 GTILNO 1.1 PCROSS 1.18
	Gilbert-Cameron	Exciton model (PCROSS)	Modified Lorentzian (MLO1)	PCROSS 0.8 ATILNO 0.9 GCROT 1.35
	Hartree-Fock-BCS	Multistep compound	Modified Lorentzian (MLO1)	ROHFBP 0.7 GDIV 5.0

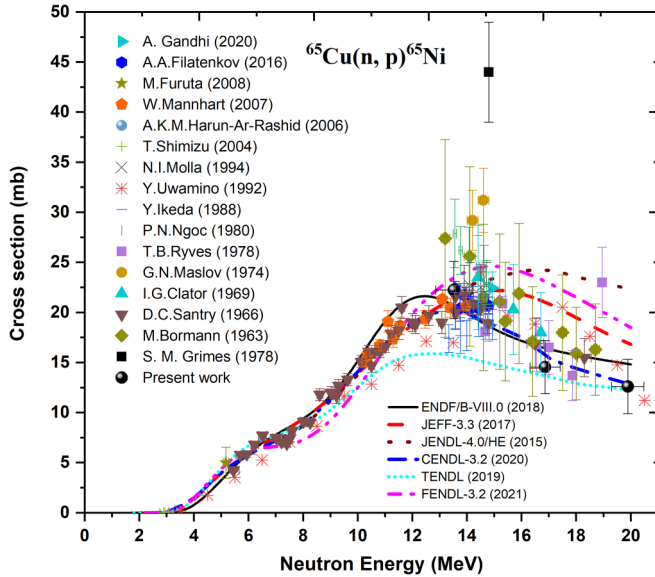


FIG. 5. Comparison of the present data with the previous measurements taken from the EXFOR compilation, data of Grimes *et al.*, and the evaluated data from the ENDF/B-VIII.0, JEFF-3.3, JENDL-4.0/HE, CENDL-3.2, TENDL-2019, and FENDL-3.2 libraries.

3.2, TENDL-2019, and FENDL-3.2 libraries [22–27] within the reaction threshold to 21 MeV neutron energy. As can be seen from Fig. 5, several measurements are available between 12 and 15 MeV and the results of the present measurements are consistent with the experimental and evaluation data. The measurements of Ryves *et al.* [16], Maslov *et al.* [17], and Santry *et al.* [19] were carried out by the NaI(Tl) detector to determine the  $^{65}\text{Cu}(n, p)^{65}\text{Ni}$  reaction cross sections. The measured cross section of Maslov *et al.* [17] is much higher than those of the six evaluated excitation curves. However, the reaction cross section predicted by Santry *et al.* [19] is varied over the entire energy region. Further, as can be seen, those recent measurements by Gandhi *et al.* [7] follow the trend of Uwamino *et al.* [21], Santry *et al.* [19], and Bormann *et al.* [20]. Our measured cross sections in the present paper at the neutron energies of 13.52, 16.86, and 19.89 MeV agree with the results of Santry *et al.* [19] within the experimental uncertainties. At the neutron energies above 19 MeV, only one measured datum is available and the present paper's result at 19.89 MeV is the second experimental evidence for the excitation curve of this cross section. Our result at 19.89 MeV can be compared with the data of Uwamino *et al.* [21]. As shown in Fig. 5, the reported Grimes *et al.* [78] cross section at 14.8 MeV is higher than the experimental data taken from the EXFOR database and evaluated data of different libraries [22–27]. It is observed that the total proton production cross section is the sum of  $(n, p)$ ,  $(n, np)$ , and other reactions channels and therefore the value of the Grimes *et al.* cross section is higher compared to the activation cross section [7–21].

In addition, the existing experimental data and the evaluated data of the ENDF/B-VIII.0, JEFF-3.3, JENDL-4.0/HE, CENDL-3.2, TENDL-2019, and FENDL-3.2 libraries from threshold to 10 MeV are in good agreement with each other

except the evaluation of the TENDL-2019 library, which shows a lower value of the cross section above the 10 MeV. However, the ENDF/B-VIII.0, JEFF-3.3, JENDL-4.0/HE, CENDL-3.2, TENDL-2019, and FENDL-3.2 libraries above 13 MeV show that the evaluated cross section differs largely in magnitude at the higher energy region. The cross section from the JENDL-4.0/HE library at higher energies is 50 to 82% higher than the TENDL-2019 evaluation. The evaluated data of the CENDL-3.2 library are in excellent agreement with the present three data points at 13.52, 16.86, and 19.89 MeV neutron energies. In contrast, the evaluated data from the TENDL-2019 library are in excellent agreement with the present measurement at only 19.89 MeV. The latest evaluated data from the JENDL-4.0/HE library are in poor agreement with the present data and with the available experimental results above 15 MeV.

## B. Comparison of the experimental data with the theoretical values based on the TALYS and EMPIRE codes using default and adjusted parameters

The statistical model calculations using the TALYS and EMPIRE codes based on the phenomenological and microscopic level density models, first with a default parameter set and then with possible parameter adjustments, were performed and results are plotted in Figs. 6 and 7. The present and previous measurements were used to validate the theoretical calculations, taking into account the various optical potential, level density, and preequilibrium models provided by both codes.

Initially, the default TALYS results for the  $^{65}\text{Cu}(n, p)^{65}\text{Ni}$  reaction cross section adopting the phenomenological and microscopic level density models are plotted in Figs. 6(a) and 6(b). The default theoretical calculations were performed for all level density models along with the Koning-Delaroché local optical potentials and Kopecky-Uhl generalized Lorentzian  $E1$   $\gamma$ -ray strength function. As can be seen from Fig. 6(a), the constant temperature model performs very well for the present paper at 13.52, and for the data reported by Filatenkov [8], Mannhart [10], and Santry [19]. In contrast, the theoretical values based on the back-shifted Fermi gas and generalized superfluid models agree with the literature data at near threshold energies. Less satisfactory performance is noticed for the generalized superfluid and back-shifted Fermi gas models in the energy region between 6 and 25 MeV. From Fig. 6(b), the calculation with the default option based on the microscopic level density models Goriely, Goriely-Hilaire, and Goriely-Hilaire Gogny diverges from the present and previous measurements at 7 to 25 MeV. The default theoretical results of all phenomenological and microscopic level density models failed to reproduce the excitation function from the threshold to 25 MeV.

Similarly, the default EMPIRE results of the  $^{65}\text{Cu}(n, p)^{65}\text{Ni}$  reaction cross section adopting the phenomenological and microscopic level density models are plotted in Figs. 6(c) and 6(d). The default theoretical calculations were performed for all level density models along with the Koning-Delaroché optical potentials, exciton preequilibrium model (PCROSS), and modified Lorentzian  $\gamma$ -ray strength function (MLO1).

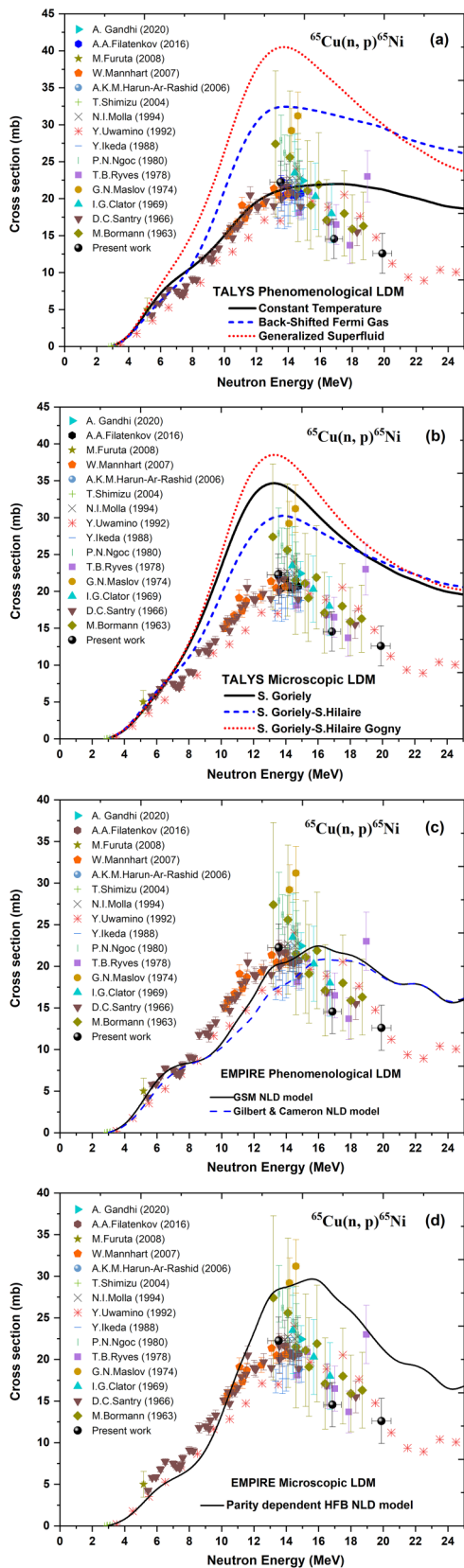


FIG. 6. The present  $^{65}\text{Cu}(n, p)^{65}\text{Ni}$  reaction cross section along with the experimental data and theoretical values based on the (a), (b) TALYS and (c), (d) EMPIRE codes with the default option.

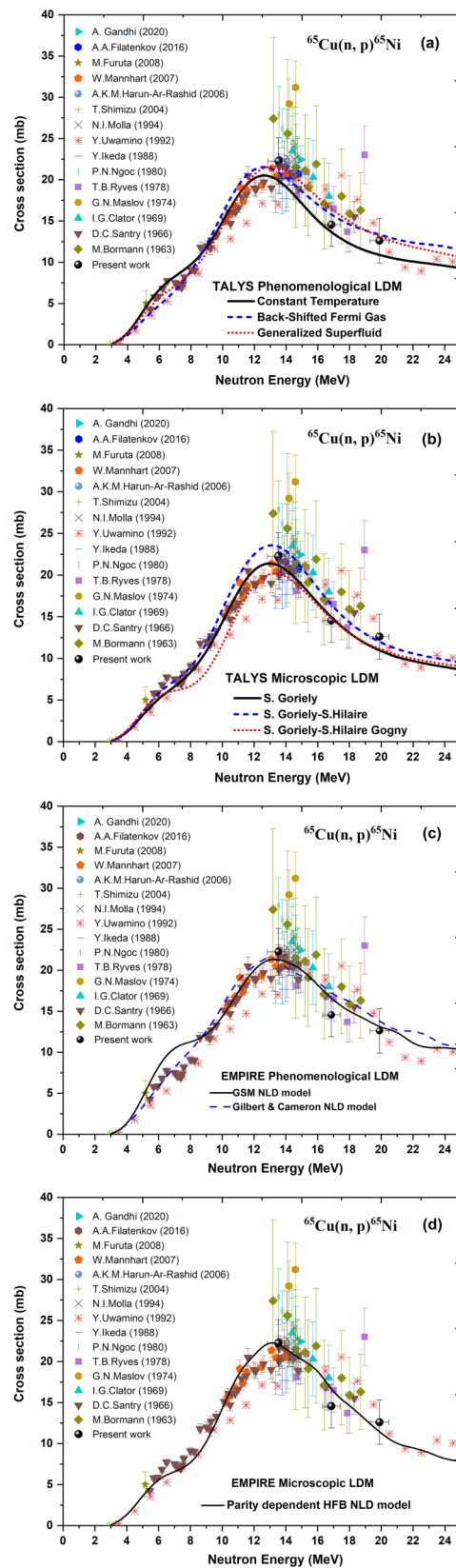


FIG. 7. The present  $^{65}\text{Cu}(n, p)^{65}\text{Ni}$  reaction cross section along with the experimental data and adjusted theoretical values obtained from the (a), (b) TALYS and (c), (d) EMPIRE codes with adjusted parameters.

The calculations from the EMPIRE code using the phenomenological level density models are shown in Fig. 6(c). These phenomenological calculations reproduced the cross sections from threshold to 8 MeV but failed to reproduce the excitation curve above 8 MeV. Furthermore, the excitation curve of the parity dependent HFM microscopic level density model is less satisfied with the present and previous measurements as shown in Fig. 6(d). The theoretical results from EMPIRE with the default option using the phenomenological and microscopic level density models failed to reproduce cross sections from threshold to 25 MeV.

In view of large discrepancies between the measured cross section and the results from the statistical model codes TALYS and EMPIRE, using default parameters for the  $^{65}\text{Cu}(n, p)^{65}\text{Ni}$  reaction, the theoretical values were revised with adjusted parameters to reproduce the experimental data more accurately. The optical potential, level density, and preequilibrium models and level-density parameters are of primary importance and have been individually adjusted to produce the previous and the present measured data. The adjusted values of the parameters and the adopted models to reproduce the measured data with statistical TALYS and EMPIRE codes are given in Tables XII and XIII. The theoretical results of modified calculations with adjusted level density parameters and models are illustrated in Fig. 7.

In TALYS calculations Figs. 7(a) and 7(b) the full  $j$ - $l$  coupling was considered in the Hauser-Feshbach theory (TALYS keyword: “fullhf”) to improve the experimental cross section. The Hofmann-Richert-Tepel-Weidenmüller model for width fluctuation corrections in compound nucleus calculations is considered in the TALYS calculations. The behavior of the constant temperature model was improved by combining the Koning-Delaroche local potential model with preequilibrium model 3 and widthmode 2. The parameters “asys” and “gshell” were enabled for this model to reproduce the experimental data. The excitation curve of the back-shifted Fermi gas model was improved by combining the optical potential of Koning-Delaroche global potential and the Kopecky and Uhl model for the  $\gamma$ -ray strength functions with widthmode 2. Furthermore, the theoretical calculations were improved when the generalized superfluid model was applied in combination with the optical potential of Koning-Delaroche global potential and the Kopecky and Uhl model for the  $\gamma$ -ray strength functions with widthmode 2. In addition, all microscopic level density models have better behavior when combined with the Koning-Delaroche global potential and preequilibrium model 3 and widthmode 2 and taking “ctable” and “ptable” values. The value of the constant  $c$  (ctable) and  $\delta$  (ptable) of the adjustment function for tabulated microscopic level densities were taken from the RIPL-3 database. In the theoretical calculations based on TALYS with default option consider these parameter values zero.

The EMPIRE code was also used to do theoretical calculations, using alternative models for optical model parametrization, level density, and  $\gamma$ -ray strength functions. The adjusted theoretical calculation based on the phenomenological models is shown in Fig. 7(c). This calculation reproduced the previous and present work by considering the different models and parameters as mentioned in Table XIII. Similarly, the

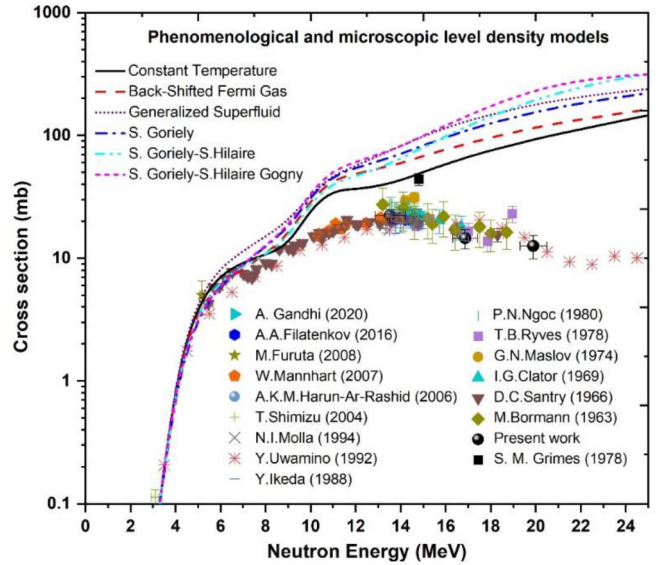


FIG. 8. Comparison of the activation cross section [7–21] and total proton emission cross sections [78] with the theoretical calculations performed by the TALYS code.

microscopic calculation based on the parity dependent HFM models was improved by combining and adjusting the values of parameters in theoretical calculations as shown in Fig. 7(d). The reduction in the preequilibrium emission contribution and adjusting the values of the parameters resulted in a more accurate reproduction of the experimental results over the whole energy range.

In addition, the theoretical calculations were performed to reproduce the data of Grimes *et al.* at 14.8 MeV using the TALYS code based on the phenomenological and microscopic level density models. The total proton production cross-section data of Grimes *et al.* [78] are reproduced by the default calculation based on the phenomenological constant temperature model as shown in Fig. 8. Moreover, the back-shifted Fermi gas and generalized superfluid phenomenological and three microscopic level density models predict higher value of the cross section.

At higher neutron energies the cross-section measurements are also interesting since the contribution of the preequilibrium mechanism to the total reaction cross section becomes important. The present measurements extend above 15 MeV incident neutron energy, and the preequilibrium processes are expected to assume significance at energies above 10 MeV. The various theoretical preequilibrium models were considered to describe a cross section of the  $^{65}\text{Cu}(n, p)^{65}\text{Ni}$  reaction at higher neutron energies. TALYS uses the exciton model based on numerical transition rates with an energy-dependent matrix element as the default choice for the preequilibrium reactions. In the present paper, the contribution of different reaction mechanisms (compound, preequilibrium, and direct) to the total reaction cross section of the  $^{65}\text{Cu}(n, p)^{65}\text{Ni}$  reaction was calculated by the TALYS code. The dominance of each reaction mechanism is illustrated in Fig. 9. As can be seen, the compound and preequilibrium mechanisms are a significant portion of reaction cross sections. Above the

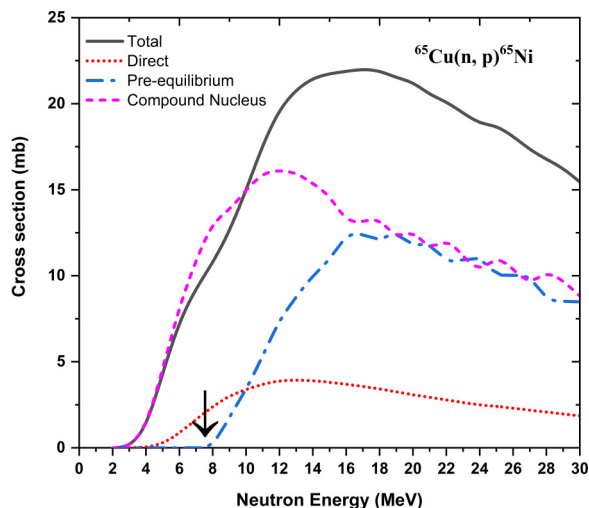


FIG. 9. The contribution of the cross section in the  $^{65}\text{Cu}(n, p)^{65}\text{Ni}$  reaction from different reaction processes (direct, preequilibrium, and compound) to the total reaction cross section was calculated using the TALYS code.

8 MeV neutron energy, the contribution of the preequilibrium emission increases with energy. Equally, it contributes to the present reaction cross section from the compound nucleus process with a minor contribution from the direct reaction.

## VII. SUMMARY AND CONCLUSIONS

In conclusion, the cross section of the  $^{65}\text{Cu}(n, p)^{65}\text{Ni}$  reaction was measured at three incident neutron energies using quasimonoenergetic neutrons produced via the  $^7\text{Li}(p, n)$  reaction. The  $^{65}\text{Cu}(n, p)^{65}\text{Ni}$  reaction cross section was measured relative to the  $^{27}\text{Al}(n, \alpha)^{24}\text{Na}$  reference reaction using the activation technique and new decay data. The correction factors are taken into consideration due to  $\gamma$ -ray self-

attenuation, geometry correction, and low energy background neutrons. The uncertainties in the measured cross sections are in the range of 13–22%. The  $(n, p)$  reaction cross section for the  $^{65}\text{Cu}$  isotope was also calculated using the systematic formulas to investigate data and validate the formulas within the 14–15 MeV neutron energy region.

Theoretical calculations were performed using the TALYS and EMPIRE codes from the reaction threshold to 25 MeV neutron energies. The present and previous measurements were used to validate the theoretical values based on the TALYS and EMPIRE codes by considering the level density, optical potential, and preequilibrium models. The impacts of various combinations of the nuclear input parameters of different level density models, optical model potentials, and preequilibrium models were also considered. The computed cross sections were found to be similar to the observed data when specific level density models were applied. Moreover, the impacts of optical model potential and  $\gamma$ -ray strength functions were much less than those of nuclear level densities. The present measurements of the  $^{65}\text{Cu}(n, p)^{65}\text{Ni}$  reaction provide important support for verifying the accuracy of nuclear models used in the calculation of cross sections and for the design and construction of fusion/fission reactors, and other related nuclear engineering calculations.

## ACKNOWLEDGMENTS

The authors gratefully acknowledge the BARC-TIFR Pelletron Accelerator Facility staff for their assistance and smooth operation of the system. R.K.S. is thankful to IUAC New Delhi for financial assistance and a fellowship through Project No. UGC-IUAC/XIII.7/UFR-60321. The authors are also grateful to S. C. Sharma (Scientific Officer, BARC-TIFR Pelletron Accelerator Facility) and the staff of the TIFR target laboratory for preparing the Li and Ta target setup, which was used for neutron flux production during the experiment.

- [1] O. K. Harling, G. P. Yu, N. J. Grant, and J. E. Meyer, *J. Nucl. Mater.* **104**, 127 (1981).
- [2] U.S. Department of Energy, Proceedings of the Workshop on Copper and Copper Alloys for Fusion Reactor Applications, 1983 (unpublished).
- [3] G. J. Butterworth, *J. Nucl. Mater.* **135**, 160 (1985).
- [4] J. B. Hicks, Toroidal field system for tight aspect ratio tokamak reactors, Culham Laboratory Report, AEA FUS Report No. 118, 1991 (unpublished).
- [5] D. L. Smith, B. A. Loomis, and D. R. Diercks, *J. Nucl. Mater.* **135**, 125 (1985).
- [6] N. Otukaa, E. Dupont, V. Semkov *et al.*, *Nucl. Data Sheets* **120**, 272 (2014).
- [7] A. Gandhi, A. Sharma, A. Kumar, R. Pachua, B. Lalremruata, S. V. Suryanarayana, L. S. Danu, T. Patel, S. Bishnoi, and B. K. Nayak, *Phys. Rev. C* **102**, 014603 (2020).
- [8] A. A. Filatenkov, R, INDC (CCP)-0460 (2016).
- [9] M. Furutaa, T. Shimizua *et al.*, *Ann. Nucl. Energy* **35**, 1652 (2008).
- [10] W. Mannhart and D. Schmidt, R, PTB-N-53 (2007).
- [11] A. K. M. Harun-Ar-Rashid *et al.*, *Indian J. Phys.* **80**, 737 (2006).
- [12] Toshiaki Shimizua, Hitoshi Sakane *et al.*, *Ann. Nucl. Energy* **31**, 975 (2004).
- [13] N. I. Molla and S. M. Qaim, *Nucl. Phys. A* **283**, 269 (1977).
- [14] Y. Ikeda, C. Konno, K. Oishi *et al.*, JAERI Report No. 1312, 1988 (unpublished).
- [15] P. N. Ngoc, S. Gueth, F. Deak, and A. Kiss, Ph.D. thesis, Eotvos Lorand Univ., Budapest Hungary, 1980.
- [16] T. B. Ryves, P. Kolkowski, and K. J. Zieba, *Metrologia* **14**, 127 (1978).
- [17] G. N. Maslov, F. Nasyrov, and N. F. Pashkin, USSR report to the INDC, 1974 (unpublished), p. 10.
- [18] I. G. Clator, Ph.D. thesis, University of West Virginia, USA, 1969.
- [19] D. C. Santry and J. P. Butler, *Can. J. Phys.* **44**, 1183 (1966).
- [20] M. Bormann, S. Cierjacks *et al.*, *Z. Phys.* **174**, 1 (1963).
- [21] Yoshitomo Uwamino, *Nucl. Sci. Eng.* **111**, 391 (1992).
- [22] D. A. Brown, M. B. Chadwick, R. Capote *et al.*, *Nucl. Data Sheets* **148**, 1 (2018).

- [23] P. Pereslavtsev, A. Konobeyev *et al.*, JEFF-3.3, Evaluation nuclear data library of the OECD Nuclear Energy Agency, JEF/DOC, 2017, p. 1864.
- [24] S. Kunieda *et al.*, Overview of JENDL-4.0/HE and benchmark calculation, JAEA Conf. Proc. No. 2016-004 (2016), pp. 41–46.
- [25] K. Xu, H. X. An, C. H. Cai, and H. C. Wu, CENDL-3.2 Chinese evaluation neutron data library, 2020.
- [26] A. J. Koning, D. Rochman, J.-Ch. Sublet *et al.*, TENDL-2019, *Nucl. Data Sheets* **155**, 1 (2019).
- [27] R. A. Forrest, R. Capote, N. Otsuka *et al.*, FENDL-3.2 Fusion Evaluation Nuclear Data Library, IAEA INDC Report No. NDS-0628, 2021 (unpublished).
- [28] R. Capote, K. I. Zolotarev *et al.*, International Reactor Dosimetry and Fusion File IRDFF v.1.05, IAEA, Technical Report No. INDC(NDS)-0616, 9 Oct. 2014 (unpublished).
- [29] A. J. Koning *et al.*, TALYS (ver. 1.9), A nuclear reaction program, user manual, NRG-1755 ZG Petten, The Netherlands (2018).
- [30] M. Herman, R. Capote, M. Sin *et al.*, *Nucl. Data Sheets* **108**, 2655 (2007).
- [31] J. F. Ziegler, *Nucl. Instrum. Methods B* **219-220**, 1027 (2004).
- [32] E. Browne and J. K. Tuli, *Nucl. Data Sheets* **111**, 2425 (2010).
- [33] R. B. Firestone, *Nucl. Data Sheets* **108**, 2319 (2007).
- [34] C. V. Midhun, M. M. Musthafa, S. V. Suryanarayana, T. Santhosh, A. Baishya, P. N. Patil, A. Pal, P. C. Rout, S. Santra, R. Kujur *et al.*, *Phys. Rev. C* **104**, 054606 (2021).
- [35] M. W. McNaughton, N. S. P. King, F. P. Brady *et al.*, *Nucl. Instrum. Methods A* **130**, 555 (1975).
- [36] J. A. Jungerman, F. P. Brady *et al.*, *Nucl. Instrum. Methods A* **94**, 421 (1971).
- [37] F. P. Brady and J. L. Romero, *Nucl. Sci. Eng.* **106**, 318 (1990).
- [38] Y. Uwamino, T. Suharti Soewarsono *et al.*, *Nucl. Instrum. Methods. A* **389**, 463 (1997).
- [39] D. L. Smith *et al.*, Corrections for low energy neutron by spectral indexing, <https://www.oecdnea.org/science/docs/2005/nsc-wpec-doc2005-357.pdf>.
- [40] T. Vidmar, *Nucl. Instrum. Methods A* **550**, 603 (2005).
- [41] D. W. Millsap and S. Landsberger, *Appl. Radiat. Isot.* **97**, 21 (2015).
- [42] W. Hauser and H. Feshbach, *Phys. Rev.* **87**, 366 (1952).
- [43] C. Kalbach, *Phys. Rev. C* **33**, 818 (1986).
- [44] A. J. Koning and M. C. Duijvestijn, *Nucl. Phys. A.* **744**, 15 (2004).
- [45] A. J. Koning and J. P. Delaroche, *Nucl. Phys. A.* **713**, 231 (2003).
- [46] E. Bauge, J. P. Delaroche, and M. Girod, *Phys. Rev. C* **63**, 024607 (2001).
- [47] R. Capote, M. Herman *et al.*, RIPL-3, *Nuclear Data Sheets* **110**, 3107 (2009).
- [48] D. M. Brink, *Nucl. Phys.* **4**, 215 (1957).
- [49] P. Axel, *Phys. Rev.* **126**, 671 (1962).
- [50] J. Kopecky and M. Uhl, *Phys. Rev. C* **41**, 1941 (1990).
- [51] A. Gilbert and A. G. W. Cameron, *Can. J. Phys.* **43**, 1446 (1965).
- [52] W. Dilg, W. Schantl, H. Vonach, and M. Uhl, *Nucl. Phys. A* **217**, 269 (1973).
- [53] A. V. Ignatyuk, K. K. Istekov *et al.*, *Sov. J. Nucl. Phys.* **29**, 450 (1979).
- [54] A. V. Ignatyuk, J. L. Weil, S. Raman, and S. Kahane, *Phys. Rev. C* **47**, 1504 (1993).
- [55] S. Hilaire, M. Girod, S. Goriely, and A. J. Koning, *Phys. Rev. C* **86**, 064317 (2012).
- [56] S. Goriely, F. Tondeur, and J. M. Pearson, *Atom. Nucl. Data Tables* **77**, 311 (2001).
- [57] S. Goriely, S. Hilaire, and A. J. Koning, *Phys. Rev. C* **78**, 064307 (2008).
- [58] J. Raynal, Computing as a language of physics, ICTP International Seminar Course, IAEA, ICTP, Trieste, Italy (1972).
- [59] H. M. Hofmann, J. Richert, J. W. Tepel *et al.*, *Ann. Phys. (NY)* **90**, 403 (1975).
- [60] J. W. Tepel, H. M. Hofmann, and H. A. Weidenmuller, *Phys. Lett. B* **49**, 1 (1974).
- [61] H. M. Hofmann, T. Mertelmeier, M. Herman, and J. W. Tepel, *Z. Phys. A* **297**, 153 (1980).
- [62] V. A. Plujko, *Acta Phys. Pol. B* **31**, 435 (2000).
- [63] H. Nishioka, J. J. M. Verbaarschot, and S. Yoshida, *Ann. Phys. (NY)* **172**, 67 (1986).
- [64] T. Tamura, T. Udagawa, and H. Lenske, *Phys. Rev. C* **26**, 379 (1982).
- [65] J. J. Griffin, *Phys. Rev. Lett.* **17**, 478 (1966).
- [66] M. Blann, *Phys. Rev. C* **54**, 1341 (1996).
- [67] J. Luo *et al.*, *Nucl. Instrum. Methods B* **266**, 4862 (2008).
- [68] R. A. Forrest and J. Kopecky, *Fusion Eng. Des.* **82**, 73 (2007).
- [69] E. Tel, B. Sarer, S. Okuducu *et al.*, *J. Phys. G: Nucl. Part. Phys.* **29**, 2169 (2003).
- [70] F. I. Habbani and Khaldia T. Osman, *Appl. Radiat. Isot.* **54**, 283 (2001).
- [71] R. Doczi, V. Semkova *et al.*, IAEA-NDS Report No. Indc (HUN)-032, 1997 (unpublished).
- [72] Y. Kasugai, Y. Ikeda, H. Yamamoto, and K. Kawade, in Proceedings of the 1994 Symposium on Nuclear Data, 1995 (unpublished).
- [73] C. Konno, Y. Ikeda, K. Osishi, K. Kawade *et al.*, JAERI Report No. 1329, 1993 (unpublished).
- [74] I. Kumabe and K. J. Fukuda, *Nucl. Sci. Tech.* **24**, 83 (1987).
- [75] S. Ait-Tahar, *J. Phys. G: Nucl. Phys.* **13**, L121 (1987).
- [76] V. M. Bychkov, V. N. Manokhin *et al.*, IAEA-NDS Report No. Indc (CCP), 1980 (unpublished), p. 146.
- [77] V. N. Levkovski, *Zh. Eksp. Teor. Fiz.* **45**, 305 (1963) [*JETP* **18**, 213 (1964)].
- [78] S. M. Grimes, R. C. Haight, K. R. Alvar, H. H. Barschall, and R. R. Borchers, *Phys. Rev. C* **19**, 2127 (1979).